A Soft Barometric Tactile Sensor to Simultaneously Localize Contact and Estimate Normal Force with Validation to Detect Slip in a Robotic Gripper

Thomas De Clercq, Anatolii Sianov, Guillaume Crevecoeur

***Abstract*— Soft tactile sensing technologies provide the potential to endow a sense of touch to robots for grasping and manipulating objects. During the execution of such tasks, having accurate knowledge on the contact location and quantitative forces in broad exerted force ranges is key. For industrial adoption such sensor needs to be low-cost, robust with limited or no calibration procedures and easy to manufacture. In this work we present a microelectromechanical (MEMS) based barometric sensor array covered with an elastomer layer, with the sensor signals being interpreted in real-time on the basis of a parameterized Gaussian type of distribution. The contact location is determined by finding in real-time the corresponding parameters of the Gaussian distribution that on its turn is used for normal contact force estimation. Results show accuracies in terms of localization of 0.5 mm and normal force errors of 10 % in force ranges up to 25 N and 15 % in high force ranges of 25 - 50 N. The proposed soft tactile sensor has furthermore been validated to provide the ability to detect slip when gripping various objects.**

I. Introduction

Over the past decade, robotic soft tactile sensing technologies emerged, finding their use in many research fields such as object feature extraction and classification [1][2], slip detection [3]–[6], dexterous in-hand manipulation [7] and telepresence [8]. Tactile sensors are particularly valuable in the localization of contacts and estimating contact forces for the purpose of grasping and manipulating fragile, lightweight and deformable objects [9].

A variety of tactile sensors exist that utilize different sensing principles: optical [10]–[15], magnetic [16][17], barometric [18]–[21], capacitive [22][23], piezo-resistive [24], electrical impedance [25], etc. Renowned commercial solutions, such as SynTouch BioTac [26] and Right Hand Robotic Takktile [27], provide state-of-the-art sensing capabilities that can be exploited by robotic grippers. Many of the above listed sensors require an extensive calibration procedure in addition to training sophisticated machine learning approaches to interpret sensor signals. These limitations can potentially hinder easy and fast embedding of tactile sensors in commercially available grippers.

The authors are with the Department of Electromechanical, Systems and Metal Engineering, Ghent University; and the Flanders Make core lab EEDT Decision and Control; Technologiepark 131, B-9052, Ghent; Email: {thomas.declercq, anatolii.sianov, guillaume.crevecoeur}@ugent.be

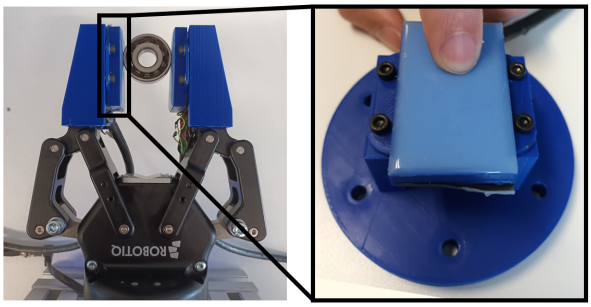

Fig. 1: Experimental setup of the presented tactile sensors mounted in the fingertips of a robotic gripper (left), Close-up of a single barometric tactile sensor being pressed with a finger (right).

In this work we present a simple, low-cost sensor to simultaneously localize and estimate normal contact forces and by embedding this sensor in an off-the-shelf gripper we demonstrate its capabilities towards detecting slip while gripping various objects. This is illustrated in Fig. 1. Our sensor consists of an array of low-cost microelectromechanical (MEMS) barometric pressure sensors covered with an elastomer layer. Recorded signals of the sensor array are interpreted using a dedicated parameterized model. The modeling approach is based on a Gaussian function containing a limited number of parameters that does not require offline data collection for calibration. Additionally it is capable to reconstruct an approximate pressure distribution over the flat sensing area using information coming from the limited number of the MEMS sensors.

The main contributions of this work are the following:

- A soft tactile sensor able to simultaneously localize point of contact and estimate normal forces (up to 50 N) in an accurate and real-time manner over a flat sensing area (648 mm^2).
- A sensor that is low-cost[1], easy to deploy and does not require an offline calibration or data-intensive machine learning procedures by assuming a Gaussian pressure distribution.
- A localization-based slip detection validated with various objects forced in a slipping condition under an externally applied load.

[1]Calculated price of the tactile sensor components is approximately 80 EUR (Excl. VAT).

II. Related Work

A. Tactile Sensors

The localization and force estimation in the fingertip of a robotic gripper is a popular research topic. A lot of different sensing principles have been explored but three types dominate the field.

The first being *vision-based* (or optical) tactile sensors. An optical device, i.e. a camera, provides high resolution information about the deformation of a soft surface when subjected to external forces [10]. To convert the high resolution information coming from the camera into meaningful data, vision-based tactile sensors rely heavily on neural networks and/or excessive calibration procedures. These sensors generally provide an accurate estimate of the position of the contact point but require a minimum focal distance leading to big, bulky sensors. The thickness of the sensor can be significantly reduced using a multi-camera approach as detailed in [10]. Optical tactile sensors are often more easily integrated in complex shaped fingertips [11][12]. As shown in [13], the neural network can also be trained using simulated data from a finite element analysis (FEA) reaching a Root Mean Square Error (RMSE) on the total force of 0.281 N at 120 Hz. The performance of these data-driven optical tactile sensors seems to be influenced by the indentation depth and the indentor shape. In [24], the localization error is significantly reduced as the indentation depth increases. The same trend is found in [15]. A probabilistic approach is one way to step away from the neural networks. In [12], a Bayesian classifier is used to localize the contact point with an accuracy of 0.1 mm in the best case. Another method to avoid a neural network is found in [14]. Here a combination of a polynomial fitting algorithm, to find the maximal depth at each marker, and Gaussian curve fitting algorithm, to find the exact contact location, is used. This resulted in a mean error around 3 mm. Despite omitting the neural network, they still require data-intensive calibrations.

The second type are the *magnetic* tactile sensors. Here, a permanent magnet is embedded in an elastic layer. When a force acts on the sensor, the elastic layer deforms and displaces the magnet. The change in the magnetic field, caused by this movement, is detected using a Hall sensor and allows to determine the contact forces [16]. Instead of using a single permanent magnet, a flexible magnetic film allows to detect the contact location and forces with a maximal error of around 0.1 mm and a RMSE of 0.01 N at frequencies of 10 Hz [17].

The last dominant sensing principle is *barometric* pressure sensing. Barometric sensors use a MEMS transducer along with integrated signal conditioning, analog-to-digital conversion, and bus interface in a standard surface-mount package [18]. When placed in a planar array, they can be used to estimate the shape and location of an object through contact with a mean location error between 0.8 mm and 2 mm [19]. Barometric pressure sensors furthermore allow to estimate contact forces. Their accuracy is significantly impacted by the orientation of the sensor. In [20], it was found that placing the sensor at a 45° angle with respect to the contact pad yields the best results. A minimal RMSE of 1.74 N was found for the normal force. To advance upon the design of barometric pressure sensor array, FEA tools can help as the configuration influences the sensing accuracy and cross-talk can be maximized [21]. Cross-talk is the phenomenon where the activation of a single sensor also produces a meaningful signal in other sensors resulting in richer pressure data which can be exploited for localization purposes. The optimal configuration provided a median error of 1.1 mm.

Besides these three main sensing principles, *capacitive* tactile force sensors exist that work on the basis of capacitance changes due to the movement of small nips [23]. To localize the contact point, Bayesian perception similar to the vision-based tactile sensors, can be used together with the capacitive sensors [22]. Using an active Bayesian perception approach, accuracies of about 0.18 mm can be reached. Also *piezo-resistive* tactile sensors exist that can localize with a median error of 0.97 mm [24]. In [25] the SynTouch BioTac is used to estimate the point of contact. The point of contact is found analytically by computing a weighted average of the changes in *impedance* of electrodes according to their Cartesian coordinates with an average error of 0.29 mm. Table I shows an overview of the required training/calibration data, localization and force errors found in the state-of-the-art.

B. Slip Detection

Generally, the localization and force estimation are done separately. In this study we propose a method with the ability to simultaneously localize contact and estimate the corresponding forces in broad force ranges. This enables various capabilities for robotic gripping and manipulation tasks that require a sense of touch e.g., slip detection. [4] gives a excellent summary of all the relevant methods and sensors used for slip detection.

Machine learning approaches have also been widely implemented in slip detection. In [5] and [6], Support Vector Machines (SVM) are used for the discrimination between static and slipping objects. If slipping is observed, the gripping force is increased to catch the object. Success-rate between 95 % [5] and 74 % [6] were reached.

Another method to estimate the slipping behaviour of an object is by processing tactile signals (via differentiation). When an object starts slipping, the stick-slip behaviour induces small vibrations with are used to predict the slipping behaviour. In [28], this is applied to detect slip by measuring changes in resistance of a composite.

Another slip detection method can be found in [23]. Here, slip is detected by observing the frequency spectrum of a capacitive tactile sensor. A success-rate of

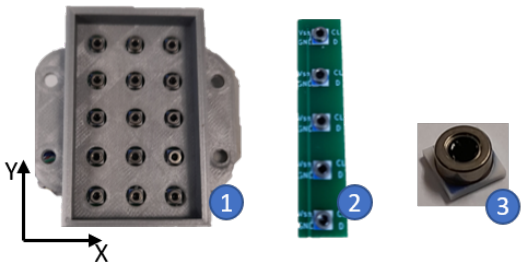

Fig. 2: Illustration of the tactile sensor components prior to rubber casting. On the left (1) we show a 3D printed holding box with PCB strips (2) glued to the bottom of the box. Finally, on the right (3) is a depiction of a single barometric MEMS sensor.

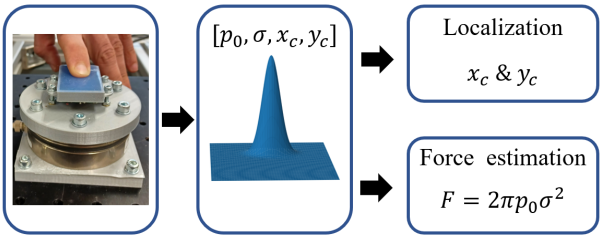

Fig. 3: Illustration of the working principle of the model-based simultaneous localization and force estimation. *Left:* Finger creates contact with the sensor. *Middle:* Optimization finds parameter values of the parameterized Gaussian pressure distribution that best fits the pressure data. *Right:* The found parameters values are used to simultaneously locate the contact and estimate forces.

94.4 % was achieved.

A fourth common method consists in comparing the tangential force to the normal gripping force. If this ratio becomes larger than the friction coefficient, the object starts slipping. Although this approach is used a lot, it is prone to changes in the environment that affect the friction coefficient.

The slip detection methodology that we propose here is based on our soft tactile sensing and we will demonstrate the capabilities of relying on contact localization. This approach does not rely on the uncertain friction coefficient nor does it require a data-intensive machine learning approach.

III. Methods

A. MEMS-Based Barometric Tactile Sensor

The core of the presented barometric tactile sensor consists of an array of digital micro altimeters (MS5840 [29]). The sensor has an exposed MEMS transducer covered with gel and a compact size (3.3 mm × 3.3 mm × 1.7 mm). The sensors are soldered to three Printed Circuit Boards (PCB) strips. Each strip holds 5 sensors. The distance between center point of the neighbouring sensor is 9 mm. A simple rectangular holding box was 3D printed (Ultimaker 2+ using Polylactic acid (PLA) material) with dimensions of 30 × 50 × 7 mm and a perforated bottom. The 3 PCB strips were glued to the bottom of the box, exposing pressure sensors through the holes (Fig. 2). Next, a soft contact elastomer layer is prepared. We use a mixture of a two component liquid elastomer, namely Resion ResinTechnology. Using a Vacuum Pump VE115SV the elastomer was degassed and poured into the sensor's holding box. In a final stage the assembled tactile sensor with elastomer layer in liquid form is degassed once more and left to be cured during 24 hours to become a solid silicon rubber. The hardness expressed via the Shore index is 15A. Degassing is a standard technique in tactile sensor manufacturing and is essential in achieving a reliable bond between the protected MEMS transducer and the elastomer [18].

B. Model-Based Localization and Force Estimation

Our approach of the model-based localization and normal force estimation is presented in Fig. 3.

A bivariate normal Gaussian distribution is used to reconstruct the pressure distribution along a rectangular surface (with Cartesian x and y coordinates) and can be

TABLE I: Comparison of state-of-the-art: Training data, localization and force errors.

Sensing principle		Requires Training data	Localization error	Force error
Optical				
	C. Trueeb et al. [10]	Yes (sample size unknown)	/	0.0571 N
	N. F. Lepora et. al. [12]	160 000 samples	0.1 - 0.5 mm	/
	C. Sferrazza et. al. [13]	135 000 samples	/	0.281 N
	J.-i. Lee et. al. [14]	No	3.4 mm	/
	P. Piacenza et al. [15]	5100 samples	0.6 mm	/
Magnetic				
	Y. Yan et al. [17]	Yes (sample size unknown)	0.1 mm	0.01 N
Barometric				
	D. Mohtasham et. al. [19]	Yes (sample size unknown)	1.4 mm	/
	C. Reeks et. al. [20]	100 000 samples	/	1.74 N
	P. Piacenza et al. [21]	1536 samples	1.1 mm	/
Capacitive				
	N. F. Lepora et. al. [22]	9000 samples	0.12 mm	/
Piezo-resisitive				
	P. Piacenza et. al. [24]	864 samples	0.97 mm	/
Electrical impedance				
	C.-h. Lin et. al. [25]	No	0.29 mm	/

formulated as

$$f(x,y) = \frac{1}{2\pi\sigma_x\sigma_y\sqrt{1-\rho^2}} e^{-\frac{1}{2(1-\rho^2)}\Delta} \tag{1}$$
$$\Delta = [(\frac{x-\mu_x}{\sigma_x})^2 - 2\rho(\frac{x-\mu_x}{\sigma_x})(\frac{y-\mu_y}{\sigma_y}) + (\frac{y-\mu_y}{\sigma_y})^2]$$

where μ_x and μ_y are the mean of x and y, σ_x and σ_y is the standard deviation in the x and y direction, ρ denotes the correlation between x and y.

Derived from (1) a pressure distribution of the following form is assumed on the tactile sensor surface:

$$p(x,y,\theta) = p_0 e^{-\frac{1}{2}\frac{(x-x_c)^2+(y-y_c)^2}{\sigma^2}} \tag{2}$$

where $p(\cdot)$ is the pressure, $\theta = [p_0, \sigma, x_c, y_c]$ are the parameters of the Gaussian, p_0 is the maximal pressure at the bottom surface, σ is the standard deviation of the Gaussian and x_c and y_c are the x- and y-coordinate of the center of the Gaussian.

An important assumption is that the standard Gaussian (1) is simplified to a symmetric Gaussian ($\sigma_x = \sigma_y = \sigma$, $\rho = 0$) and that the proportionality term p_0 in (2) relates to the maximal pressure value exerted on the bottom surface.

Under these assumptions, the localization problem can be reformulated into a minimization problem that fits the best Gaussian distribution (2) to the measured pressure data. The following error function is minimized:

$$Err(\theta) = \sum_{i=1}^{n} [p(x_i, y_i, \theta) - \widehat{p}_i]^2 \tag{3}$$

where $p(\cdot)$ is the estimated pressure, x_i and y_i are the x- and y-coordinate of sensor i, $\theta = [p_0, \sigma, x_c, y_c]$ are the parameters of the Gaussian. The $\widehat{p}_i$ are the measured pressure values (components of measurement vector $\widehat{\mathbf{p}}$).

To increase the efficiency of the algorithm, we only look at the n largest pressure values obtained from the pressure readings. Increasing n, results in an improvement of the accuracy but also reduces the speed of the optimization.

The parameters are found with a least-squares optimization method resulting in an optimal θ^* value. This gives us the location of the center of the Gaussian which is per definition also the contact point.

The information to localize the contact point can be used to determine the normal forces in the contact area. Integration of the pressure distribution (2) with respect to x and y leads to the following expression:

$$\begin{aligned} F_z &= \iint p(x,y,\theta^*)\,\mathrm{d}x\,\mathrm{d}y \\ &= 2\pi p_0 \sigma^2 \end{aligned} \tag{4}$$

As both parameters (p_0 and σ) have been estimated, the force can be easily calculated.

C. Force Controller with Slip Detection

To illustrate the capabilities of the model-based localization and normal force estimation, this subsection describes a force controller based on the force estimation and a slip detection based on the localization which can be run simultaneously.

When mounting the tactile sensor at the fingertips of a gripper, the grasping force during gripping is estimated using (4). The use of a PID controller allows us to control the applied gripper force with a previously position-controlled gripper using following equations:

$$e_f = F_{z,des} - \frac{F_{z,l} + F_{z,r}}{2} \tag{5}$$

$$\Delta P = k_d e_f + k_i \int e(\tau) d\tau + k_d \dot{e}_f \tag{6}$$

where e_f is the gripping force error, $F_{z,des}$ is the desired gripping force, $F_{z,l}$ and $F_{z,r}$ are the estimated gripping forces at the left and right fingertip (note, it is expected that $F_{z,l} \approx F_{z,r}$), ΔP is the desired position change of the fingertips, k_d is the proportional gain, k_i is the integral gain and k_d is the derivative gain.

The knowledge of the location of the contact point can be used to develop a localization-based slip controller. By comparing the most recent contact location with the location found in the previous n time-steps, it is possible to detect if an object is slipping. Following metric is defined:

$$\epsilon_i = \sqrt{(x_i - \frac{x_{i-1} + ... + x_{i-n}}{n})^2 + (y_i - \frac{y_{i-1} + ... + y_{i-n}}{n})^2} \tag{7}$$

where ϵ_i is the slip distance, x_i and y_i are the estimated x- and y-coordinate of the contact at time-step i and n is the number of previous time-steps. When ϵ_i is larger than a predefined threshold value ϵ_{thres}, the contact is considered to be slipping.

IV. Results & Discussion

A. Data Collection and Processing

An extensive data collection campaign was conducted to assess the accuracy of the localization and normal force estimation. Different poking trajectories were generated using a robot arm (Universal Robot 5e). The UR5e was controlled using the MoveIt! motion control package in a ROS environment (ROS Noetic patched with a Preemptive Linux kernel). Data was collected according to an equidistant grid with a spacing of 4.5 mm in both x- and y-directions (Fig. 4b) resulting in 21 sample locations (3×7 grid). The robot was also programmed to collect data at random positions. The UR5e is position-controlled and provides the actual location of the contact point (x, y) (pose repeatability of 0.03 mm).

The poking trajectories executed by the UR5e use one of the four 3D-printed indentors shown in Fig. 4a attached to the end-effector. There is the small spherical

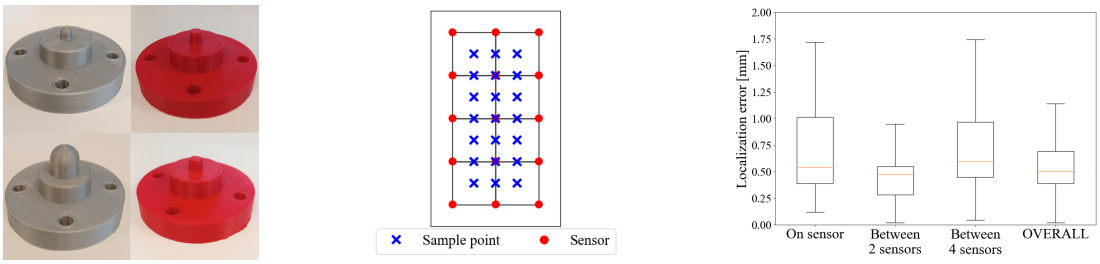

(a) Indentors (b) Sampling grid (c) Localization error: Sampling grid

Fig. 4: Evaluation of the model-based localization accuracy when using the different indentors (a) for various samples distributed along a regular grid (b). The accuracy (c) is assessed by comparing the recorded (x,y) positions (position-controlled UR5e) to the positions estimated from the signals originating from the tactile sensor.

(a) Ball Bearing (b) Bottle Cap (c) Lime (d) Ping-Pong Ball (e) Rubber Duck

Fig. 5: Set of the 5 test objects.

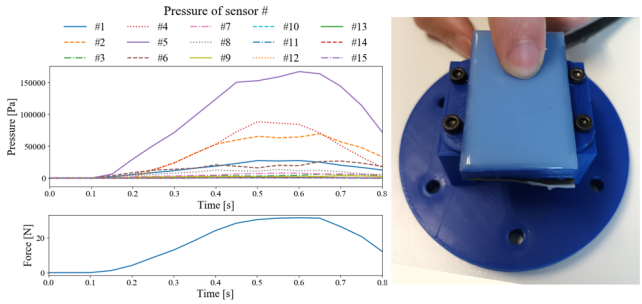

Fig. 6: Pressure signals collected from the MEMS-based sensor array and measured force when poking near sensor 5.

indentor (d = 6 mm), the large spherical indentor (d = 15 mm), the cylindrical indentor (d = 6 mm) and the cubical indentor (l = 6 mm). During the poking trajectories, a 6-DoF ATI M80-M8 force/torque sensor collected the forces and torques in all 3 spacial directions. We kept record of the normal forces F_z (resolution of 0.04 N). Besides only tapping on the sensor using the UR5e with the indentors, the sensor was also manually poked with 5 random objects with varying size and deformability. In this study a ball bearing, a bottle cap, a lime, a Ping-Pong ball and a rubber duck were used (Fig. 5).

The tactile sensor outputs 15 scalar pressure values (Fig. 6) at 20 Hz. These are arranged into a vector $\widehat{\mathbf{p}}$. Note that the pressure values $\widehat{\mathbf{p}}$ collected from the barometric sensors need be set to zero between each contact event. An additional implementation detail is that the position readings and force sensor readings are downsampled to 20 Hz as these are sampled at higher frequencies (up to 500 Hz) than the pressure data. A total of 40,000 samples were collected with each sample containing $[\widehat{\mathbf{p}}, x, y, F_z]$.

These samples are used to assess the accuracy of the localization and force estimation by comparing the directly measured contact location (x, y) with the model-based localization (2) having parameter values θ^* from minimizing (3). Similarly, the directly measured F_z values are compared with the model-based force estimation (4). The video attachment further demonstrates the performance of the tactile sensor.

B. Localization: Error evaluation

The model-based localization error is evaluated with the small and large spherical indentor according to the detailed data collection from Section IV.A with the grid sampling depicted in Fig. 4b. The results on the localization errors of both indentors are combined in Fig. 4c.

At first, the position of the indentor w.r.t. the position of the individual sensors is investigated. When the indentor is positioned right above a single sensor (on a red dot in Fig. 4b) a median error of 0.54 mm is found. However when it is positioned between 2 sensors (on a black line in Fig. 4b) a median error of 0.48 mm is found and a median error of 0.59 mm was found for the cases in which the indentor is positioned between 4 sensors (in the center of the white squares in Fig. 4b). This results in an overall median error of 0.51 mm. In all three cases the median error is sufficiently close to the overall median error to conclude that the accuracy is uniform in the entire domain.

Next, these results are compared to the results of the random tapping. As described in section IV.A, the robotic arm is used to poke the sensor at random locations with the poking force varying from 1 N to 15 N with one of the four indentors. All results are summarized in Table II. It should be noted that the error of the cubical indentor is slightly higher than the other indentors. This can be explained by the fact that the pressure distribution is no longer a symmetrical Gaussian.

Nonetheless, our tactile sensor achieves a lower localization error (localization error: 0.48 mm - 0.85 mm) than the ones found with other barometric tactile sensors in the state-of-the-art (localization error: 1.1 mm - 1.4 mm).

C. Force estimation: Error evaluation

As detailed in section III.B, the presented model-based sensor array does not only provide the capability to locate the contact point but also to simultaneously

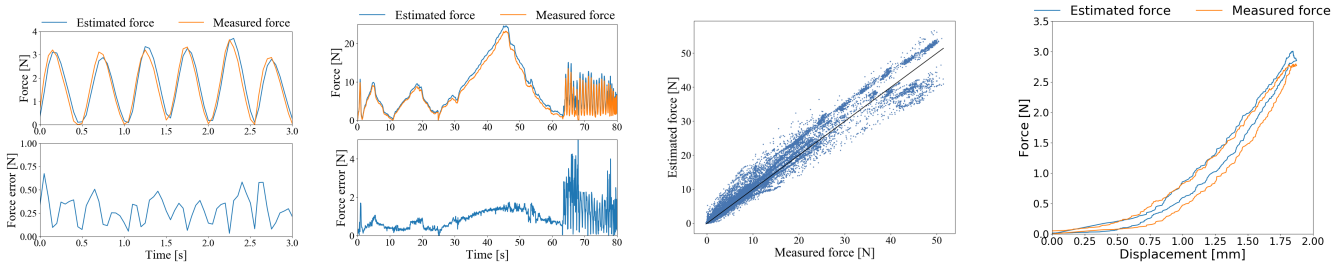

(a) (b) (c) (d)

Fig. 7: Comparison of directly measured forces with the ATI F/T-sensor (orange) and model-based force estimations (blue) with (a) UR5e with small spherical indentor (b) Ping-Pong ball, (c) All collected data points, (d) The quasi-static response when poked with the small spherical indentor.

TABLE II: Overall median error and standard deviation (STD) of the localization for the different test cases.

	Median error [mm]	STD [mm]
Sampling grid		
Small spherical indentor	0.55	0.84
Large spherical indentor	0.48	0.33
Random tapping		
Small spherical indentor	0.52	1.42
Large spherical indentor	0.53	0.26
Cylindrical indentor	0.55	0.70
Cubical indentor	0.85	0.98

estimate the contact force (4). The force estimation was evaluated using the collected data from Section IV.A.

Fig. 7a provides a comparison on the measured and estimated forces on the data collected with the UR5e. The Root Mean Square Error (RMSE) achieved by the algorithm during this task is 0.54 N and the Median Absolute Percentage Error (MAPE) is 4.5 %. Besides executing this repetitive movement we also poked the sensor manually to evaluate the force estimation in a more dynamic environment. The sensor was poked with 5 random objects (Fig. 5). These objects lead to pressure distributions which are different from the assumed symmetric Gaussian. Despite not completely satisfying this assumption, an RSME of 1.49 N and MAPE of 10.2 % is found in a force range of 0 - 25 N (Fig. 7b). Nonetheless the accuracy is comparable to the accuracy found using the UR5e. This demonstrates the ability of the presented sensing methodology to estimated forces in dynamic environments with various non-ideal objects.

To assess the robustness, we furthermore apply forces to the sensor which are far above the conventionally working area when handling fragile objects. When the sensor is loaded up to 50 N, the estimation error increases to a RMSE of 4.67 N and a MAPE of 15.7 %. This can be attributed to the pressure sensors coming close to saturation as well as the elastomer behaving outside the linear regime. Note that the localization in such high force range (25 - 50 N) does not deteriorate compared to low force as this saturation primarily influences the parameters used to estimate the force (p_0 and σ). The above results suggest that the sensor is versatile and performs well for low and higher force ranges while simultaneously locating and estimating contact forces.

Fig. 7c shows the measured forces (using the ATI F/T-sensor) and compares it with the estimated forces. This for all 40,000 data samples (Section IV.A). This figure shows the correspondence of the model-based force estimation with the actual force measurements exhibiting only a limited spread. A higher spread can be observed in the larger force regions. The correlation coefficient r of 0.985 is found, supporting the validity of using (4) as a model-based force sensor.

Additionally the quasi-static response of the tactile sensor is compared to the response of the ATI F/T-sensor (Fig. 7d). In both cases, the response exhibits a hysteresis loop and is non-linear. This is due to the elastomer contact pad and the use of a spherical indentor. This quasi-static behavior of the tactile sensor is similar to the behavior of the ATI F/T-sensor and further validates the model-based force estimation.

D. Slip detection: Error evaluation

To assess the performance of the slip detection we altered the setup. Firstly, the sensors are now mounted on the fingertips of a position-controlled robotic gripper (Robotiq 2F-85). This makes it possible to grasp an object (Fig. 5) with a predefined, object-specific gripping force (5)-(6). This is also illustrated at the left side of Fig. 1. This holding force is kept constant during the entire experiment though continuous actuation. Afterwards a poker is mounted on the ATI F/T-sensor, at the end-effector of the UR5e robotic arm (Fig. 8a). Using the UR5e, the poker can apply an external load on the object forcing it into a slipping state. To determine if an object is truly slipping, 2 conditions need to be satisfied: 1) there is contact between the poker and the object 2) the poker is moving. Condition 1 is validated by observing the data from the ATI F/T-sensor mounted on the poker. Condition 2 is easily checked because of the known position of the end-effector. This allows us to identify the true slipping behaviour of the object. To determine the accuracy of the slip detection (7), the output of the sensors are compared to this true slipping behaviour. We opted to represent the accuracy as a success-rate because both a false-positive (a static object labeled as slip) and a false-negative (a slipping object labeled as static) would

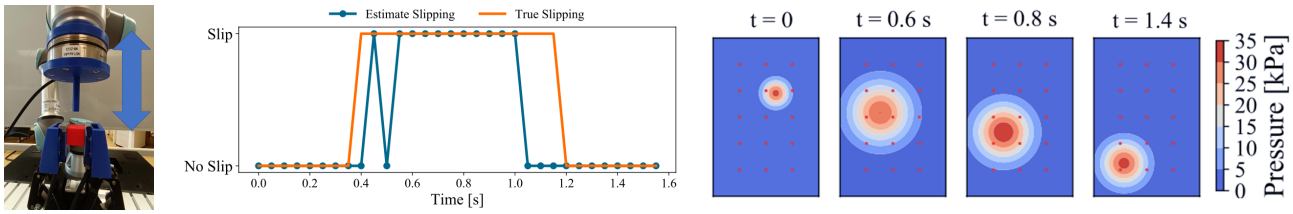

(a) (b) (c)

Fig. 8: (a) Experimental setup slip detection, (b) Estimated slip vs True slipping behavior - Success-rate: 84.4 %, (c) Reconstructed pressure distribution during the slip experiment on the tactile sensor.

TABLE III: Average success-rate of the slip detection for each object with $n = 2$ and $\epsilon_{thres} = 0.75$ mm.

Object	Success-rate	STD
Ball Bearing	82.3 %	5.2 %
Bottle Cap	82.7 %	7.7 %
Lime	82.6 %	8.8 %
Ping-Pong Ball	78.3 %	9.9 %
Rubber Duck	79.7 %	7.4 %
OVERALL	81.1 %	8.2 %

result in failure. These experiments are also included in the video attachment to this paper.

The slip detection experiments are done with the 5 objects used in Section IV.C at 5 slipping speeds ranging from 20 mm/s to 200 mm/s. Each experiment was repeated 3 times resulting in 75 experiments. The results of a single experiment is shown in Fig. 8b. Table III shows to results of the slip detection (7) with $n = 2$ and $\epsilon_{thres} = 0.75$ mm.

The single slip experiment (Fig. 8b) indicates that sensors correctly identify the slipping behavior for 27 time-steps, but there are also 5 time-steps for which an estimation is wrong (i.e. all false-negatives). This leads to a success-rate of $27/(27+5) = 0.844$ or 84.4 %. Fig. 8c shows the changing pressure distribution during this slip experiment. This clearly illustrates the movement of the estimated Gaussian pressure distribution which is used to identify slip.

An overall average success-rate of 81.1 % was found with little difference between the 5 objects. This shows that the slip detection is capable of identifying the slipping behaviour correctly for a range of objects with different contact shapes. This performance is also invariant to changes in material properties as this significantly varies throughout the objects. Similarly the size of the objects suggests limited influence on the success-rate. When using $n = 2$ and $\epsilon_{thres} = 0.75$ mm the slip detection is not affected by the slipping speed. However by increasing n, the success-rate at the slowest slipping speed marginally improves but success-rates at higher slipping speeds significantly reduces leading to an overall worse success-rate.

Similar experiments were conducted using a set of spheres, cylinders and cubes (Fig. 9) which were varied in size (diameter and/or length of 12 mm - 18 mm - 24 mm). The results are summarised in Table IV. Similar success-rates as Table III were found. In the case of a cube, which was shown to have a slightly worse localization

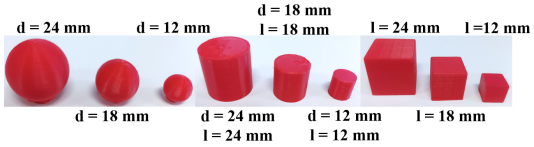

Fig. 9: Set of spheres, cylinders and cubes of different sizes.

TABLE IV: Success-rate of the slip experiments with arbitrary objects

	Small	Medium	Large	Average
Sphere	80.5 %	85.4 %	82.0 %	82.6 %
Cylinder	78.9 %	77.5 %	81.1 %	79.2 %
Cube	84.0 %	76.9 %	77.6 %	79.6 %

accuracy, the sensor is still capable of predicting the correct slipping behavior.

It is important to note that these success-rates are lower than found in literature. However in this study, the success-rate is calculated based on the slipping behaviour at every time interval (of 0.05 s), rather than a single measure for the entire time-series.

V. Conclusions & Future Work

A tactile sensor was presented capable to localize contacts and estimate normal forces over a flat surface. To demonstrate the capabilities of the localization, a localization-based slip detection was developed. The MEMS sensor readings are interpreted using a parameterized Gaussian model that reconstructs the pressure distribution. The presented methodology does not require offline data collection opposed to data-driven approaches that need sufficient training data. An additional advantage of the presented tactile sensor is the ease of assembling and manufacturing as well as its low cost.

The contact location is found by fitting a Gaussian pressure distribution model to the pressure signals. This can be done in real-time at 20 Hz. These parameters are also used to estimate the normal forces. Extensive evaluations have been carried out to assess the accuracy of the model-based approach in terms of localization and normal force estimation. Results show localization errors in the the range of 0.5 mm and normal force estimation errors in the range of 10 % of the applied force for relatively low force ranges (up to 25 N) and deficiencies of normal force estimations of 15 % in high force ranges (25 - 50 N). Additionally the localization and force estimation are incorporated into a force controller with slip detection (average success-rate of 81.1 %) tested with various objects forced into a slipping state under

an external load enforced by the UR5e. Furthermore the ease of manufacturing, the robustness and the absence of a calibration procedures are discussed in the paper. These attributes are key to promote industrial adoption of tactile sensors for providing a sense of touch for robotic grasping and manipulation tasks.

The presented work holds some limitations. Due to the assumption of a symmetrical 2D Gaussian, a complex shaped indentor will not achieve the same accuracy as indicated in this study. Furthermore, in case multiple contact points act simultaneously upon the sensor, the presented sensor will not be able to distinguish the different contact points. However using an iterative approach might resolve this issue.

The sensor design can furthermore be advanced upon. The spacing between the different pressure sensors needs to be further examined. The spacing can be varied to achieve a higher degree of cross-talk that can lead to more meaningful signals during contact. This allows us to reconstruct more complex pressure distributions compared to the symmetric 2D Gaussian distribution that we are limited by with the currently presented sensor arrangement. Additionally, expanding the model to capture different features (e.g., tangential force, indentation depth and torque) can be explored.

As near future research we also foresee the possibility to integrate this slip detection into a slip controller. The knowledge of the contact location allows us to deduce the slipping direction and speed. This can be exploited to for instance do in-hand repositioning of objects in robotic manipulation.

References

[1] B. S. Homberg, R. K. Katzschmann, M. R. Dogar, and D. Rus, "Haptic identification of objects using a modular soft robotic gripper," in *2015 IEEE/RSJ International Conference on Intelligent Robots and Systems (IROS)*, pp. 1698–1705, IEEE, 2015.

[2] F. Von Drigalski, M. Gall, S.-G. Cho, M. Ding, J. Takamatsu, T. Ogasawara, and T. Asfour, "Textile identification using fingertip motion and 3d force sensors in an open-source gripper," in *2017 IEEE International Conference on Robotics and Biomimetics (ROBIO)*, pp. 424–429, IEEE, 2017.

[3] Y. Karayiannidis, C. Smith, D. Kragic, *et al.*, "Adaptive control for pivoting with visual and tactile feedback," in *2016 IEEE International Conference on Robotics and Automation (ICRA)*, pp. 399–406, IEEE, 2016.

[4] R. A. Romeo and L. Zollo, "Methods and sensors for slip detection in robotics: A survey," *IEEE Access*, vol. 8, 2020.

[5] J. W. James, N. Pestell, and N. F. Lepora, "Slip detection with a biomimetic tactile sensor," *IEEE Robotics and Automation Letters*, vol. 3, pp. 3340–3346, oct 2018.

[6] J. W. James and N. F. Lepora, "Slip detection for grasp stabilization with a multifingered tactile robot hand," *IEEE Transactions on Robotics*, vol. 37, no. 2, pp. 506–519, 2020.

[7] A. Wilson, S. Wang, B. Romero, and E. Adelson, "Design of a fully actuated robotic hand with multiple gelsight tactile sensors," 2020.

[8] S. Jia and V. J. Santos, "Tactile perception for teleoperated robotic exploration within granular media," *ACM Transactions on Human-Robot Interaction (THRI)*, vol. 10, no. 4, pp. 1–27, 2021.

[9] L. Zaidi, J. A. Corrales, B. C. Bouzgarrou, Y. Mezouar, and L. Sabourin, "Model-based strategy for grasping 3d deformable objects using a multi-fingered robotic hand," *Robotics and Autonomous Systems*, vol. 95, pp. 196–206, 2017.

[10] C. Trueeb, C. Sferrazza, and R. D'Andrea, "Towards vision-based robotic skins: a data-driven, multi-camera tactile sensor," in *2020 3rd IEEE International Conference on Soft Robotics (RoboSoft)*, pp. 333–338, IEEE, 2020.

[11] B. Romero, F. Veiga, and E. Adelson, "Soft, round, high resolution tactile fingertip sensors for dexterous robotic manipulation," in *2020 IEEE International Conference on Robotics and Automation (ICRA)*, pp. 4796–4802, IEEE, 2020.

[12] N. F. Lepora and B. Ward-Cherrier, "Superresolution with an optical tactile sensor," in *2015 IEEE/RSJ International Conference on Intelligent Robots and Systems (IROS)*, IEEE.

[13] C. Sferrazza and R. D'Andrea, "Sim-to-real for high-resolution optical tactile sensing: From images to 3d contact force distributions," 2020.

[14] J.-i. Lee, S. Lee, H.-M. Oh, B. R. Cho, K.-H. Seo, and M. Y. Kim, "3d contact position estimation of image-based areal soft tactile sensor with printed array markers and image sensors," *Sensors*, vol. 20, no. 13, p. 3796, 2020.

[15] P. Piacenza, K. Behrman, B. Schifferer, I. Kymissis, and M. Ciocarlie, "A sensorized multicurved robot finger with data-driven touch sensing via overlapping light signals," *IEEE/ASME Transactions on Mechatronics*, vol. 25, no. 5.

[16] C. Ledermann, S. Wirges, D. Oertel, M. Mende, and H. Woern, "Tactile sensor on a magnetic basis using novel 3d hall sensor-first prototypes and results," in *2013 IEEE 17th International Conference on Intelligent Engineering Systems (INES)*, pp. 55–60, IEEE, 2013.

[17] Y. Yan, Z. Hu, Z. Yang, W. Yuan, C. Song, J. Pan, and Y. Shen, "Soft magnetic skin for super-resolution tactile sensing with force self-decoupling," *Science Robotics*, vol. 6, no. 51.

[18] J. W. Guggenheim, L. P. Jentoft, Y. Tenzer, and R. D. Howe, "Robust and inexpensive six-axis force–torque sensors using mems barometers," *IEEE/ASME Transactions on Mechatronics*, vol. 22, no. 2, pp. 838–844, 2017.

[19] D. Mohtasham, G. Narayanan, B. Calli, and A. J. Spiers, "Haptic object parameter estimation during within-hand-manipulation with a simple robot gripper," in *2020 IEEE Haptics Symposium (HAPTICS)*, pp. 140–147, IEEE, 2020.

[20] C. Reeks, M. G. Carmichael, D. Liu, and K. J. Waldron, "Angled sensor configuration capable of measuring tri-axial forces for phri," in *2016 IEEE International Conference on Robotics and Automation (ICRA)*, pp. 3089–3094, IEEE, 2016.

[21] P. Piacenza, S. Sherman, and M. Ciocarlie, "Data-driven super-resolution on a tactile dome," *IEEE Robotics and Automation Letters*, vol. 3, no. 3, pp. 1434–1441, 2018.

[22] N. F. Lepora, U. Martinez-Hernandez, M. Evans, L. Natale, G. Metta, and T. J. Prescott, "Tactile superresolution and biomimetic hyperacuity," *IEEE Transactions on Robotics*, vol. 31, no. 3, pp. 605–618, 2015.

[23] T. M. Huh, H. Choi, S. Willcox, S. Moon, and M. R. Cutkosky, "Dynamically reconfigurable tactile sensor for robotic manipulation," *IEEE Robotics and Automation Letters*, vol. 5, no. 2.

[24] P. Piacenza, E. Hannigan, C. Baumgart, Y. Xiao, S. Park, K. Behrman, W. Dang, J. Espinal, I. Hussain, I. Kymissis, *et al.*, "Touch sensors with overlapping signals: Concept investigation on planar sensors with resistive or optical transduction," 2018.

[25] G. E. Loeb, "Estimating point of contact, force and torque in a biomimetic tactile sensor with deformable skin," 2013.

[26] "Syntouch." https://syntouchinc.com/. [Online; Accesed 13-Sept-2021].

[27] "Right hand robotics." https : / / www . righthandrobotics .com/. [Online; Accesed 13-Sept-2021].

[28] J.-K. Lee, H.-H. Kim, J.-W. Choi, K.-C. Lee, and S. Lee, "Development of direct-printed tactile sensors for gripper control through contact and slip detection," *International Journal of Control, Automation and Systems*, vol. 16, pp. 929–936, mar 2018.

[29] "Ms5840-02ba low profile pressure sensor." https://www.te.com/usa- en/product- CAT-BLPS0060.html/. [Online; Accesed 13-Sept-2021].